Chapter 4
Thermally stable bismuth-activated Tb^{3+} doped $CaMoO_4$ green phosphor

"Chapter 4 describes the role of Bi^{3+} ions in the green luminescence of $CaMoO_4$:5%Tb^{3+} phosphors. $CaMoO_4$, Tb^{3+} (2% to 6%) doped $CaMoO_4$ and Bi^{3+} (2% to 5%) co-doped 5% Tb^{3+} doped $CaMoO_4$ samples prepared by urea-assisted combustion synthesis method. Structural and morphological analysis of all the samples has been studied and their crystalline phase, lattice strain, crystalline size and particle size have been discussed. In this chapter, the improvement in crystallinity due to doping of Bi^{3+} ions is explained and correlated with the luminescence of $CaMoO_4$:5%Tb^{3+} green phosphor. This chapter discusses the charge transfer between the energy levels of Bi^{3+} ion to Tb^{3+} ion. Moreover, the thermal stability of the best Bi^{3+} co-doped phosphor has also been investigated."

4.1 Introduction

Lanthanide (Ln^{3+}) ion-doped inorganic phosphors are being studied by researchers for the past two decades owing to their potential applications in lighting devices (wLEDs, luminescent lamps) and display devices, etc [111–113]. The wLEDs have achieved more attraction by fraternity due to their outstanding properties like environmental compatibility, low power consumption, longer lifetime, high luminous efficacy, etc [18,114,115]. The commercial wLED devices are fabricated by YAG: Ce^{3+} yellow phosphor which is deposited on InGaN blue chip [66–68]. However, white light obtained from commercial wLED has some drawbacks such as high correlated color temperature (>5000 K) which is not comfortable for the human eye and low color rendering index (<75). These deficiencies can be overcome by the conjunction of red, green and blue phosphors [116,117]. An excellent red phosphor is developed in Chapter 3. Therefore, a component green phosphor is now required for optimal white light emission.

Many inorganic phosphors have been studied for display and light emission applications, but many well-known phosphors like CaF_2, $Ca_3Si_2O_4N_2$, $CaSrAl_2SiO_7$, Ca_2SiO_4, $Ca_2Si_5N_8$, $Y_3Al_5O_{12}$, etc have some constraints such as complex synthesis methods, poor luminescence, and low chemical/thermal stability [20,118–121]. The Molybdates such as $CaMoO_4$, have good properties like environment friendliness, stable crystal structure, broad excitation band in the near-UV region, broad emission band in the full visible spectrum, longer decay life time (~14 ms), higher melting point (~ 1480 ^oC), good thermal and chemical stability [45,89,105]. Moreover, it can be easily prepared by various synthesis techniques such as the salvo/hydrothermal method, solid-state process, auto-combustion method, co-precipitation method, and sol-gel method, etc [22,77,122–125]. The urea-based auto-combustion method is profitable over other synthesis techniques due to its

cost-effectiveness. Therefore, $CaMoO_4$ is superior to other phosphors because of these properties.

The emission of $CaMoO_4$ can be tuned via different Ln^{3+} doping due to their different 4f electronic configuration [18]. Among all Ln^{3+} ions, the Tb^{3+} ion doped phosphor is applied as a green phosphor for display devices, fluorescent tubes and LEDs applications [126,127]. Many Tb^{3+} doped sulfide compounds such as Gd_2O_2S: Tb^{3+} [128], ZnS: Tb^{3+} [129], La_2O_2S: Tb^{3+} [130], Y_2O_2S: Tb^{3+}/Eu^{3+} [131], etc have been previously reported for display device applications, but have one major drawback. The sulfide compounds have poor chemical stability due to which it decomposes when high-energy electrons are exposed to them, and the luminous efficiency is reduced [132]. The sulfur element obtained after decomposition is extremely harmful to the environment and also to humans. Therefore, it is worthwhile to fabricate Tb^{3+} doped $CaMoO_4$ novel phosphors having high chemical and thermal stability and excellent luminous efficiency. The intra f transition of Tb^{3+} doped $CaMoO_4$ phosphor results in three major emission peaks at 489 nm, 544 nm, and 621 nm under near-UV radiation, which is related to Tb^{3+} transitions from $^5D_4$ exciting level to the ground levels ^7F_J (J=3,5, and 6), respectively [72,97]. The transition $^5D_4 \rightarrow {}^7F_5$ obtained at 544 nm is the strongest emission peak, leading to the overall emission green region. Generally, the Bi^{3+} ion is used as an excellent sensitizer, so the intensity of the intra f transitions of the lanthanide ions can be enhanced via doping of the Bi^{3+} ion [133]. The Bi^{3+} ion absorbs the UV radiation through the $^1S_0 \rightarrow {}^3P_1$ excitation transition and provides energy to the lanthanide activators, resulting in emission intensity enhancement [134,135]. Thus, the green emission of Tb^{3+} doped $CaMoO_4$ can be enhanced by the doping of Bi^{3+} ions.

In this chapter, the emission of Tb^{3+} doped $CaMoO_4$ phosphor was improved through Bi^{3+} co-doping. Moreover, the energy transfer mechanism from $[MoO_4]^{2-}$ ion to Bi^{3+}/Tb^{3+} ions and from Bi^{3+} ion to Tb^{3+} ion is studied. Along with it the correlation between structural and optical study is also investigated. The Tb^{3+} emission at 544 nm has been achieved maximum upon 4% Bi^{3+} co-doping. Thus, 4% Bi^{3+} co-doped $CaMoO_4$:5%Tb^{3+} has excellent green emission making it an effective green emitting phosphor for applications such as display devices and LEDs.

All the phosphors developed in this chapter are prepared by the urea-assisted internal combustion process, which has been described in detail in Chapter 2, in addition, all the characterization techniques and their models used in this chapter have been described in Chapter 2.

4.2 Results and discussion

4.2.1 XRD analysis

The Rietveld refined XRD patterns of T0, T5, and B4 samples are shown in Fig. 4.2(a-c), and obtained parameters from refinement are listed in Table 4.1. Some prominent diffraction peaks such as (101), (112), (004), (200), (212), (204), (220), (116), (312), (224) are exhibited in the figure which is well-matched with JCPDS file # 85–1267 (a=b=5.223 Å, c=11.429 Å) [45]. The XRD patterns verify that the crystal structure of all phosphors is tetragonal with space group $I4_1/a$, and its 3D structure is formed by $[MoO_4]$ tetrahedral clouds and $[CaO_8]$ dodecahedral clouds linked by common edge Ca–O–Mo as shown in Fig. 4.2(d). The lattice parameters and volume of the unit cell have been obtained by refined data using FULLPROF software [137] and tabulated in Table 4.1. The lattice parameters of the T0 phosphor are a=5.225 Å, c=11.430 Å, and the unit cell volume of T0 is 312.0461 $Å^3$. The volume of a unit cell and lattice parameters of the Tb^{3+} doped samples are decreased, with increasing concentration of Tb^{3+} ions which

may be due to the ionic radius of Tb^{3+} (1.04 Å) being less than the Ca^{2+} ion ionic radius (1.12 Å) [87]. Thereafter Bi^{3+} co-doping in Tb^{3+} doped $CaMoO_4$ phosphor increases the value of unit cell volume and lattice parameters, because the ionic radius (1.17 Å) of Bi^{3+} ion is greater than the radius of Ca^{2+} ion (1.12 Å). The variation in the volume of unit cell of all phosphors ensures that Tb^{3+} and Bi^{3+} ions take the place of Ca^{2+} ion sites.

We have calculated the crystallite size and lattice strain of the samples using Williamson-Hall (W-H) expression [138]. The well-known expression of the W-H method is given below;

$$\beta_{cal} cos\theta = 4\epsilon sin\theta + \frac{K\lambda}{D} \quad 4.1$$

Where θ is the angle of diffraction peak, β_{cal} is the calculated full width at half maximum (FWHM) of diffraction peak at a particular angle θ corrected by reducing instrument broadening. λ and K are the wavelength of the used X-ray (1.54 Å) and the shape factor (~0.9), respectively. The $\beta_{cal} cos\theta$ versus $sin\theta$ graph in the W–H expression shows a linear equation, whose intercept gives the estimated crystallite size (D) and the slope gives the estimated lattice strain (ϵ). The estimated value of D for the T0 sample is ~74 nm, which is increasing with increasing concentration of Tb^{3+} ions and further increases upon Bi^{3+} co-doping in the T5 sample. The calculated crystallite size of the prepared samples is listed in Table 4.1. The increasing crystallite size on Bi^{3+} co-doping indicates that increases the crystallinity of the samples and thereby decreases the density of the grain boundaries as similarly reported by Chauhan *et al* [135]. Hence the defects associated with grain boundaries decrease and luminescence increase [139].

The lattice strain (ϵ) represents distortion in crystal, known as lattice defects. The estimated value of ϵ for the T0 sample is 0.0036, decreasing with doping of Tb^{3+} ions and further decreasing with co-doping of Bi^{3+} ions in the T5 sample. The calculated strain value of all prepared samples is tabulated in Table 4.1. The decrement in lattice strain ascertains that lattice defects are reducing due to Bi^{3+} co-doping, which is an important factor in increasing the luminescence [135].

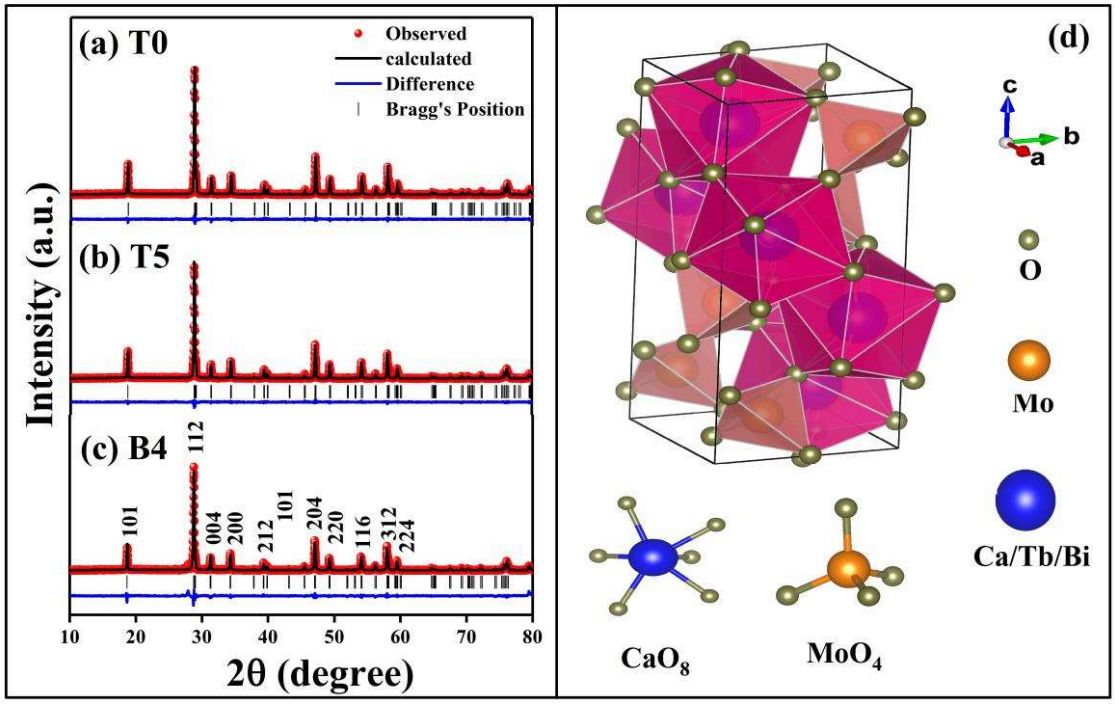

Fig. 4.1 Rietveld refined XRD patterns of **(a)** T0, **(b)** T5, **(c)** B4 samples, and **(d)** crystal structure of the B4 sample.

Table 4.1 Structural parameters obtained from Rietveld refinement XRD patterns.

Parameters	T0	T5	B4
Lattice parameter (a, c) (Å)	a=5.225, c=11.430	a=5.224, c=11.425	a=5.231, c=11.444
Ca (x, y, z)	Ca (0, 0.25, 0.625)	Ca (0, 0.25, 0.625)	Ca (0, 0.25, 0.625)

Mo (x, y, z) O (x, y, z)	Mo (0, 0.25, 0.125) O (0.1521, -0.0027, 0.208)	Mo (0, 0.25, 0.125) O (0.1516, 0.0021, 0.2075)	Mo (0, 0.25, 0.125) O (0.1511, -0.0019, 0.206)
V ($Å^3$)	312.0461	311.7903	313.1463
χ^2	3.27	3.21	6.9
Crystallite size (nm)	74	77	81
Lattice strain (10^{-4})	36	6.4	4.2

4.2.2 SEM and EDX analysis

Fig. 4.3 depicts the SEM images of the T0, T5, and B4 samples to study their morphology. These images show the spherical shape of the phosphors, which is an agglomeration of particles caused by metallic or/and covalent bonds affecting the doped ions [18]. The average size of particles was calculated via ImageJ software. The obtained particle sizes for the T0, T5 and B4 phosphors are 1.74 µm, 1.92 µm and 3.8 µm, respectively, which refers that the particle size is increasing with Bi^{3+} co-doping. Since the increase in particle size indicates an increase in crystallinity, therefore, it can be stated that the crystalline nature of the phosphor is increasing with Bi^{3+} co-doping.

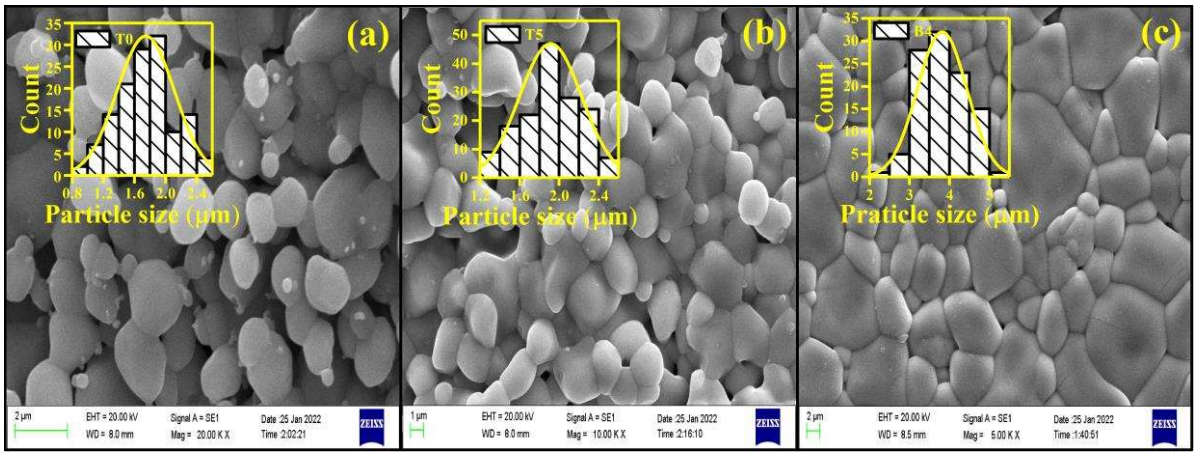

Fig. 4.2 SEM images of **(a)** T0, **(b)** T5, and **(c)** B4 samples.

The elemental composition in the samples has been investigated via EDX analysis, as depicted in Fig. 4.4, which varify the presence of all element in T0, T5, and B4 samples. It is clear from the EDX spectra that the samples do not contain any foreign impurities. The weight (Wt.) and atomic (At.) percentages as obtained from the EDX spectra and taken during the synthesis method are listed in Table 4.2.

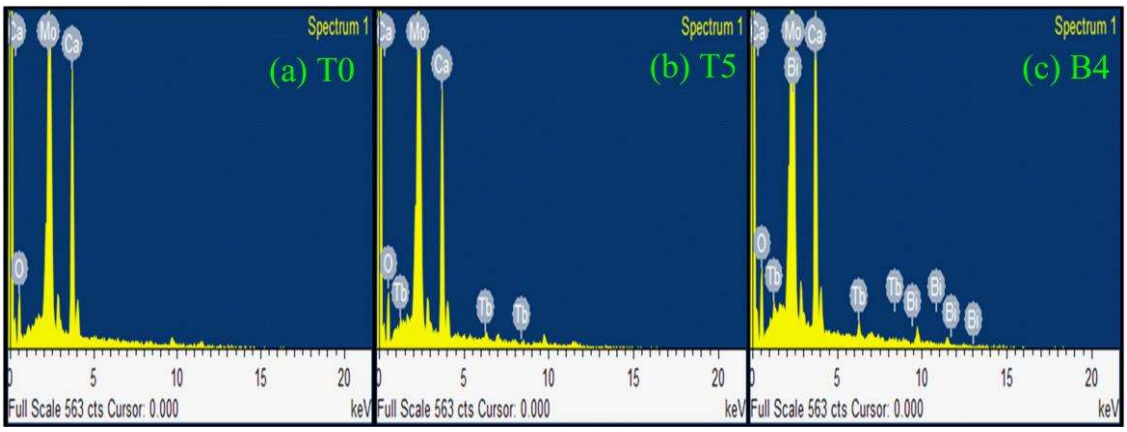

Fig. 4.3 EDX spectra for **(a)** T0, **(b)** T5, and **(c)** B4 samples.

Table 4.2 Comparative study of weight % and atomic % obtained from EDX with the taken amount used in synthesis.

Elements		EDX data		Taken amount	
		Wt. %	**At. %**	**Wt. %**	**At. %**
T0	**Ca**	21.95	19.22	20.03	16.67
	Mo	48.46	17.43	47.97	16.67
	O	29.59	63.35	32	66.67
T5	**Ca**	19.06	18.37	18.48	15.83
	Mo	49.13	19.06	46.58	16.67
	O	27.84	61.59	31.07	66.67
	Tb	3.97	0.98	3.86	0.83
B4	**Ca**	18.20	16.26	17.15	15.17
	Mo	47.11	18.30	45.11	16.67
	O	26.53	63.65	30.08	66.67
	Tb	4.39	1.02	3.73	0.83
	Bi	3.77	0.76	3.93	0.67

4.2.3 XPS analysis

The XPS scan has been performed to investigate the chemical state of all the elements present in T5 and B4 samples, as depicted in Fig. 4.5. The XPS survey scan shows the peaks corresponding to the binding energies of calcium, molybdenum, oxygen, terbium, and bismuth, Fig. 4.5(a). XPS scans of the elements are shown in Fig. 4.5(b - f). Fig. 4.5(b) depicts two bands at 350.38 eV and 346.88 eV corresponding to the energy states $2p_{1/2}$ and $2p_{3/2}$ of Ca2p, indicating that the calcium ions have a +2 oxidation state in samples. The XPS scan of Fig. 4.5(c) yields two bands at 235.58 eV and 232.38 eV which are responsible for the bound levels $3d_{3/2}$ and $3d_{5/2}$ of Mo3d core. These binding energies confirm the Mo^{6+} chemical state in the

samples. The binding energy band obtained at 530.18 eV in Fig. 4.5(d) represents the lattice oxygen of the O1s core which verifies the -2 oxidation state of oxygen in all samples. The binding energies of the core levels of calcium, molybdenum, and oxygen match well with earlier reported papers [18,91,136]. Two bound energy bands are observed centered at 1276.18 eV and 1240.98 eV in Fig. 4.5(e) corresponding to $3d_{3/2}$ and $3d_{5/2}$ levels of Tb3d core, indicating that terbium is in the +3 oxidation state in both samples [140,141]. The XPS scan of the bismuth present in the B4 sample is shown in Fig. 4.5(f). In this, two energy bands related to the Bi4f core levels of $4f_{5/2}$ and $4f_{3/2}$ are obtained in 163.98 eV and 158.68 eV. These binding energies confirm the +3 chemical state of bismuth [142]. Thus, the chemical states of all the elements present in samples T5 and B4 are confirmed with the help of respective XPS spectra.

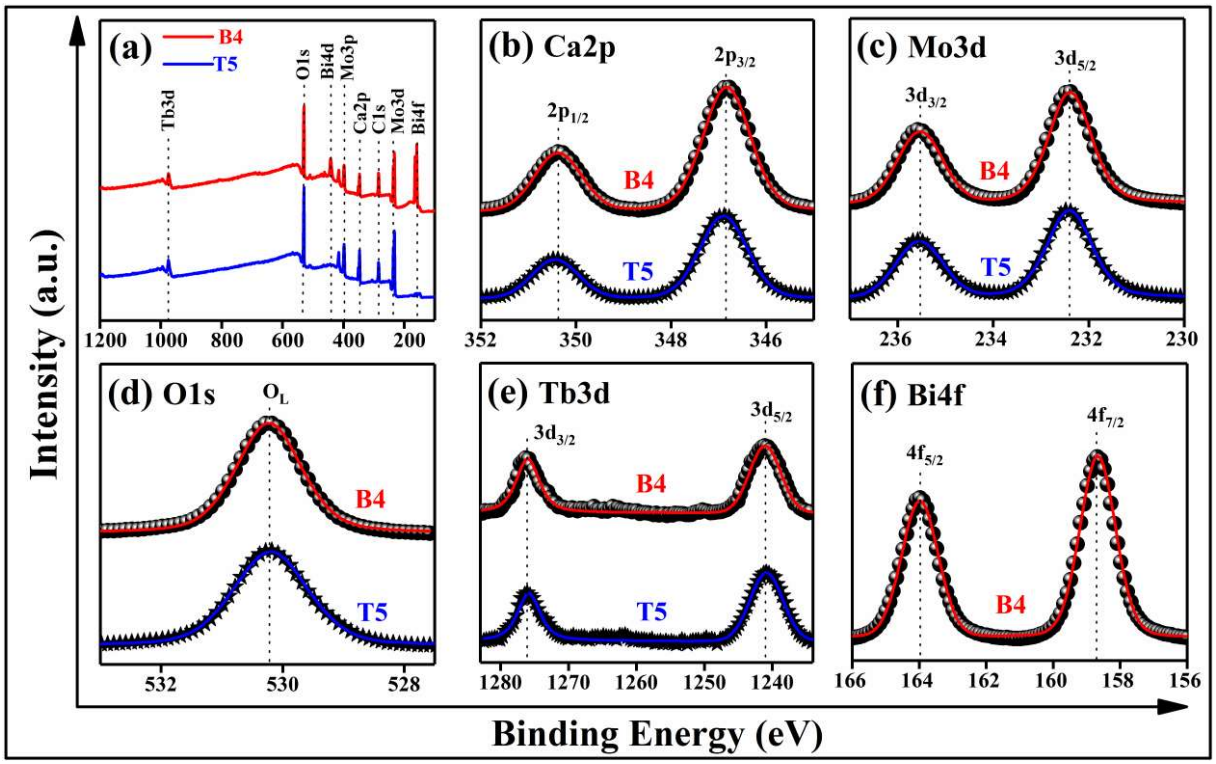

Fig. 4.4 (a) High-resolution XPS survey, XPS spectra of **(b)** Ca2p, **(c)** Mo3d, **(d)** O1s, **(e)** Tb3d and **(f)** Bi4f for B4 and T5 samples.

4.2.4 FTIR analysis

The vibrational modes present in T0, T5, and B4 samples were examined by FTIR spectra, which are shown in Fig. 4.6. Crystal structures like $CaMoO_4$ have 26 modes which can be expressed by the following equation [96],

$$\Gamma = \left(3A_g + 5A_u\right) + \left(5B_g + 3B_u\right) + \left(5E_g + 5E_u\right) \quad 4.2$$

Out of which 8 ($4A_u + 4E_u$) are IR active and 13 ($3A_g + 5B_g + 5E_g$) are Raman active vibration modes. Moreover, two vibration depths centered at 425.71 cm^{-1} and 769.77 cm^{-1} of $[MoO_4]^{2-}$ have been observed within the fingerprint range (400 cm^{-1} to 1400 cm^{-1}), responsible for bending of Mo–O bond and anti-symmetry stretching of O–Mo–O bond, respectively [97,143]. These vibration bands are attributed to A_u and E_u modes. Thus, the IR vibration band obtained from the FTIR analysis confirms the bonds of $[MoO_4]^{2-}$ clouds in samples. Another depth is observed at 2361 cm^{-1} for all samples, which is related to O=C=O band stretching vibrations, which would have been obtained due to atmospheric CO_2 molecules [98,143].

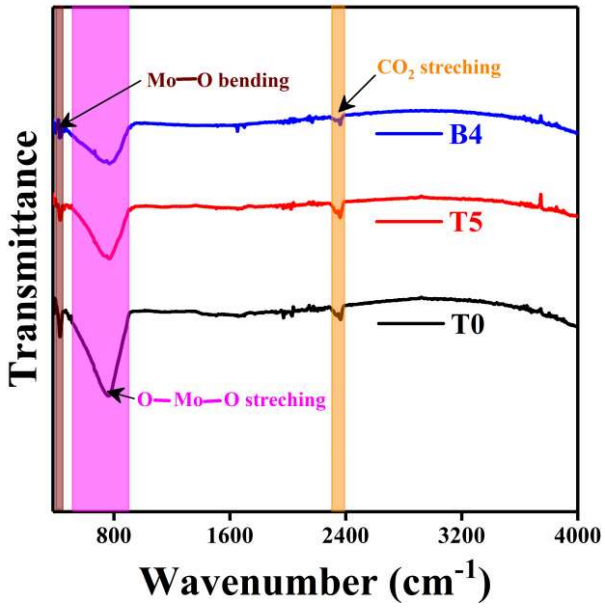

Fig. 4.5 FTIR spectra for T0, T5, and B4 samples.

4.2.5 Absorption analysis

The absorption spectra of all samples over the range of wavelength from 200 to 800 nm are shown in Fig. 4.7(a). An absorption band for the T0 centered at 298 nm is observed, due to the charge transfer band (CTB) between O^{2-} to Mo^{6+} [35]. The absorption center has shifted towards a higher wavelength at 309 nm in the Tb^{3+} doped sample; thereby the optical bandgap reduces. The increased broadness of the absorption band for Tb^{3+} doped phosphor is attributed to the overlapping of CTBs between O^{2-} to Mo^{6+} and O^{2-} to Tb^{3+}. After Bi^{3+} co-doping, the absorption peak is red-shifted and peaks at 323 nm. The absorption width further increases, which is the result of the overlapping of CTBs between O^{2-} to Mo^{6+}, O^{2-} to Tb^{3+} and O^{2-} to Bi^{3+}. A similar red shift of the peak at doping of Bi^{3+} is mentioned in Wang *et al* [133].

The optical bandgaps of all prepared samples are evaluated via 'Wood and Tauc' expression [144];

$$(\alpha h\nu)^{\frac{1}{n}} = A(h\nu - E_g) \quad 4.3$$

Where α and ν are the absorption coefficient and frequency of the incident photon. h and A are Planck constant and proportional constant, respectively. Since the transitions for $CaMoO_4$ are of the direct allowed transitions. Hence, the value of the exponent n is ½ [145]. The $(\alpha h\nu)^2$ versus $h\nu$ plot represents a linear equation whose intercept for $(\alpha h\nu)^2 = 0$ on the x-axis gives the calculated optical bandgap of all prepared samples, as depicted in inset of Fig. 4.7(a). The calculated optical band gap for the T0 sample is 3.85 eV. A reduction in the bandgap up to 3.52 eV is observed for T5 in the Tb^{3+} doped samples. Tb^{3+} ions form intermediate defect levels below the host's conduction band that reduce the bandgap [18,145]. After Bi^{3+} co-doping into the T5 phosphor, the bandgap further decreases to 3.44 eV. A similar reduction in bandgap by doping of Bi^{3+} ions has been mentioned in Yadav *et al* [146]. The bismuth ions also form an energy defect level below the conduction band of the host which further narrows the bandgap. As a result, effective energy transfers from the $[MoO_4]^{2-}$ energy level to the Bi^{3+} excited level easily occur.

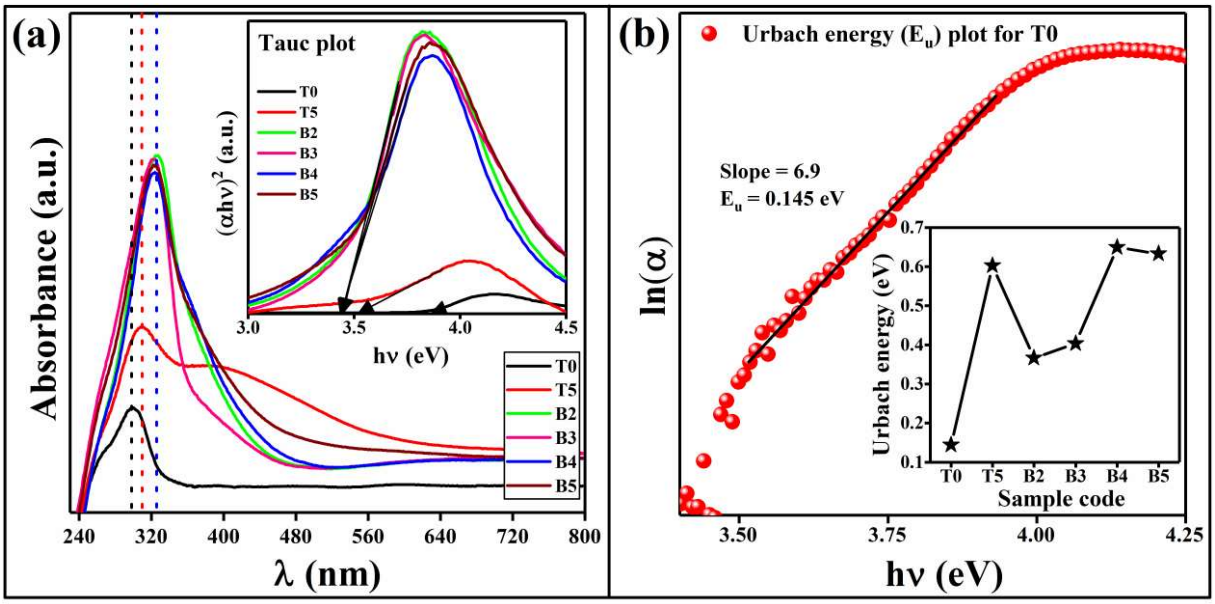

Fig. 4.6 (a) Absorption spectra for T0, T5, B2, B3, B4, and B5 samples. Inset: Tauc plot for calculation of band gap and **(b)** Plot of Urbach energy for T0 sample. Inset: Variation in Urbach energy with Bi^{3+} co-doping.

After doping of Tb^{3+}/Bi^{3+} ions, the defect levels forms in the lattice due to the mismatch of ionic radii of Ca^{2+} ion and Tb^{3+}/Bi^{3+} ions in the $CaMoO_4$ matrix, creating localized states between the bandgap. The Urbach energy indicates the formation of localized states in between the bandgap. The Urbach energy (E_U) can be calculated via Urbach Empirical formula [147,148];

$$\ln(\alpha) = \ln(\alpha_o) + \frac{h\nu}{E_U} \qquad 4.4$$

Plot $\ln(\alpha)$ versus $h\nu$ represents a linear equation as depicted in Fig. 4.7(b) for the T0 sample whose inverse of the slope gives the Urbach energy (E_U). The variation of E_U is shown in the inset of Fig. 4.7(b). The Urbach energy of the T0 sample is 0.145 eV. The E_U value increases with the doping of Tb^{3+} up to the T5 sample ($E_U = 0.60\ eV$) and increases with Bi^{3+} doping up to the B4 sample ($E_U = 0.65\ eV$), which is a verification of localized states formation within the host bandgap. A similar trend in E_U is reported in our earlier work [135].

4.2.6 Photoluminescence analysis

4.2.6.1 Excitation (PLE) spectra

The photoluminescence excitation (PLE) spectra for all the prepared phosphors are shown in Fig. 4.8. The PLE spectrum of the T0 phosphor is recorded for the host emission at 500 nm. The PLE spectra of all remaining Tb^{3+}/Bi^{3+} doped phosphors are analyzed for the intense emission of Tb^{3+} ions at 544 nm. A broadband has been observed near 287 nm for the T0 sample as depicted in Fig 4.8(a), which is responsible for a ligand to metal charge transfer (LMCT) band from 2p filled O^{2-} orbit to partially filled Mo^{6+} orbit [89]. For Tb^{3+} doped samples, these broadband width increase with the doping of Tb^{3+} ions, which results from the overlapping of the LMCT band and the charge transfer band (CTB) of the Tb^{3+} ion [23,97]. Moreover, another excitation band centered at 323 nm is observed in the Bi^{3+} co-doped phosphor as shown in Fig. 4.8(b), which results from the Bi^{3+} excitation transition $^1S_0 \rightarrow {}^3P_1$. Similar observations have been reported in previous papers [149,150]. This excitation band explains the formation of intermediate energy levels of Bi^{3+} ions within the $[MoO_4]^{2-}$ band, which facilitates energy transfer from $[MoO_4]^{2-}$ to Tb^{3+} ions.

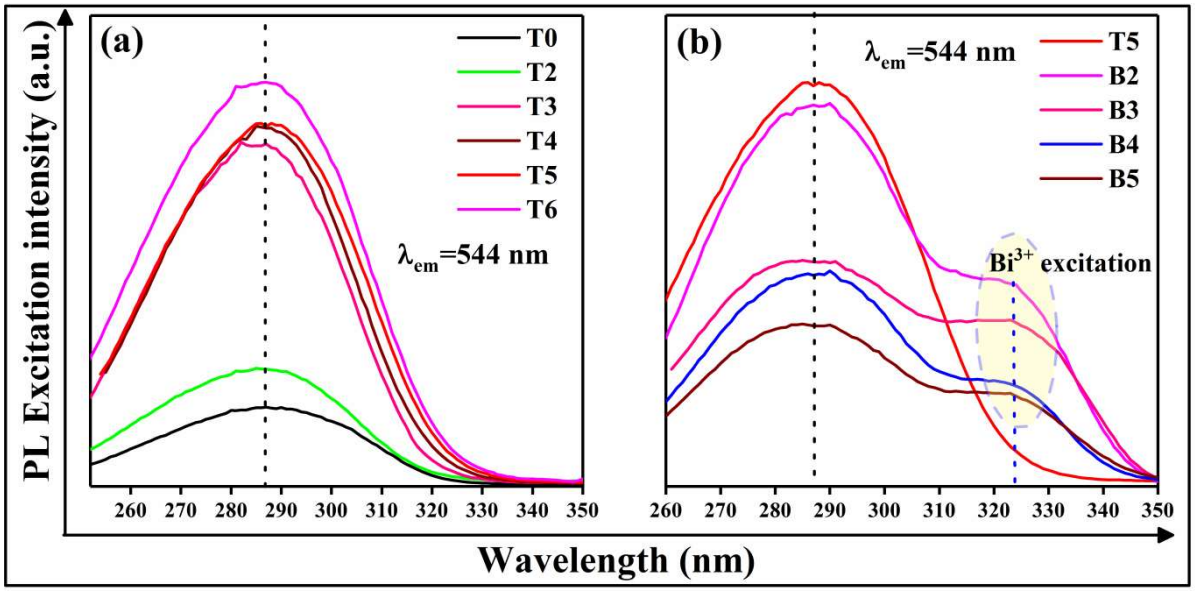

Fig. 4.7 (a) PL excitation spectra for all Tb^{3+} doped phosphors and **(b)** PL excitation spectra for all Bi^{3+} co-doped phosphors**.**

4.2.6.2 Emission (PL) spectra

The photoluminescence emission (PL) spectra of all phosphors have been analyzed under host excitation (287 nm) and are shown in Fig. 4.9. A broad emission band centered at 500 nm has been obtained for the T0 phosphor, results from charge transfer from the exciting levels to the ground level of the $[MoO_4]^{2-}$ ions, as shown in the inset of Fig. 4.9(a). Three major peaks centered at 489 nm (blue), 544 nm (green), and 621 (red) are observed in Tb^{3+} doped phosphors, which correspond to Tb^{3+} ion transitions $^5D_4 \rightarrow {}^7F_6$, $^7F_5$ and $^7F_3$, respectively [23,151]. The Tb^{3+} transition $^5D_4 \rightarrow {}^7F_6$ obtained at 489 nm is an electric dipole (ED) transition and the Tb^{3+} transition $^5D_4 \rightarrow {}^7F_5$ obtained at 544 nm is a magnetic dipole (MD) transition. The MD transition of Tb^{3+} ions is less sensitive to the surrounding chemical environment of Tb^{3+} ions, whereas the ED transition is sensitive but not hyper-sensitive. The intensity of dipole transition depends on both the ligand nature and its sensitivity to the surrounding chemical environment

[151]. It can be seen in Fig. 4.9(a) that the MD transition at 544 nm is more intense than the ED transition at 489 nm, which suggests that the Tb^{3+} ions are not strongly affected by the surrounding chemicals. This transition intensity increases with increasing Tb^{3+} concentration under host excitation, showing an energy transfer from higher levels of $[MoO_4]^{2-}$ ion to exciting levels of Tb^{3+} ion and a maximum attained for a 5% Tb^{3+} doped phosphor. After that, the intensity quenches as the concentration increases. This quenching phenomenon is caused by the overlapping of the wave functions of the activator (Tb^{3+}) ions and/or due to the multi-polar interaction of the activator ions. The critical distance between the activator ions must be less than or equal to 5 Å for the overlapping of wave functions [13]. The critical distance (R_C) of activator ions has been evaluated by Blasse formula [152];

$$R_C = 1.24\sqrt[3]{\left(\frac{V}{C\times N}\right)} \qquad 4.5$$

Where C (=0.05) is the critical concentration of Tb^{3+} ions. N (=4) is the number of lattice points per unit volume for the $CaMoO_4$ matrix. V (=311.7903 $Å^3$) is the unit cell volume for critical concentration doped phosphor which is obtained by XRD pattern analysis. The evaluated R_C value for the T5 phosphor is 14.38 Å which is higher than 5 Å, indicating that the intensity quenching is because of only the multi-polar electric interaction of Tb^{3+} ions.

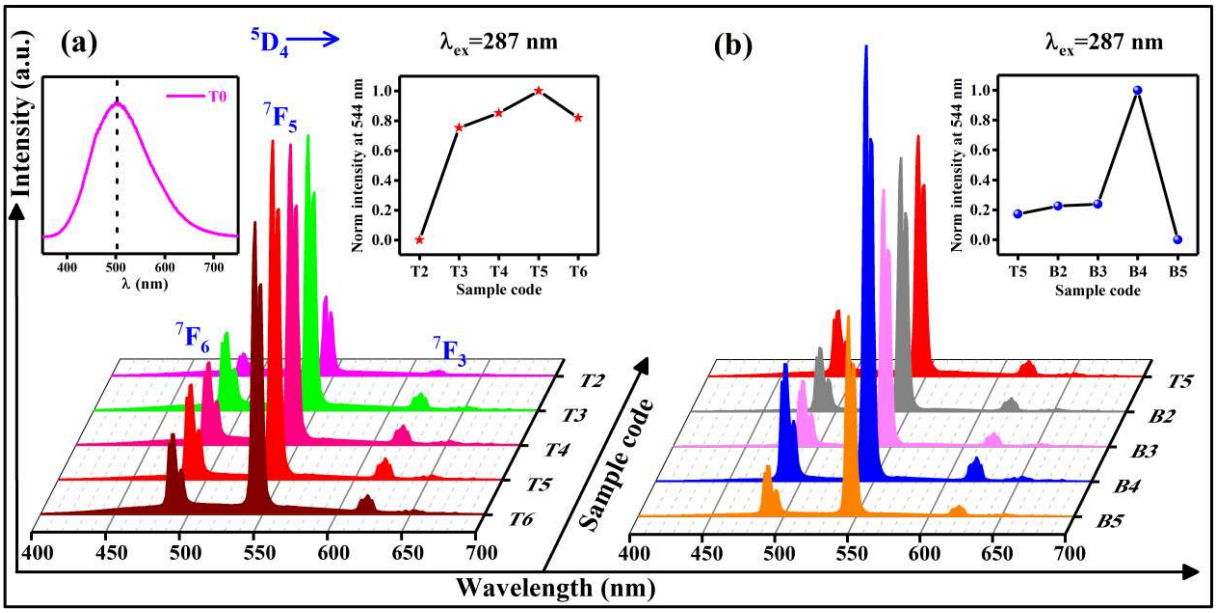

Fig. 4.8 (a) PL emission spectra for all Tb^{3+} doped phosphors and **(b)** PL emission spectra for all Bi^{3+} co-doped phosphors.

Fig. 4.9(b) represents the PL emission spectra of Bi^{3+} co-doped in the T5 sample. The intensity of emission peaks increases steadily after Bi^{3+} doping under host excitation and the maximum is achieved for 4% Bi^{3+} co-doping which is 47% higher than the overall emission intensity of T5 phosphor. The normalized intensity variation for the Tb^{3+} emission peak at 544 nm with Bi^{3+} doping is shown in the inset of Fig. 4.9(b). After that, quenching occurs on further co-doping of the Bi^{3+} ion. To identify the quenching process, the critical distance (R_C) for B4 phosphor is calculated using the above Blasse formula. The total critical concentration (C) for B4 is 0.09 and the unit cell volume (V) obtained from the XRD study is 313.1463 $Å^3$. The calculated critical distance (R_C) value for Bi^{3+} co-doped phosphor is 11.84 Å which is more than 5 Å. Therefore, we can say that the decrease in intensity by non-radiative relaxation is a result of the multi-polar interaction of Tb^{3+} ions. Multi-polar electric interactions are mainly

dipole-to-dipole, dipole-to-quadrupole and quadrupole-to-quadrupole types of interactions, whose type can be determined by Dexter's formula [153];

$$\left(\frac{I}{x}\right) = Ax^{n/3} \qquad 4.6$$

Where, x is the total doping concentration of Tb^{3+} and Bi^{3+} ions in Bi^{3+} co-doped $CaMoO_4$:5%Tb^{3+} phosphors. I is the PL intensity of Tb^{3+} ions with related doping concentration x. A is a proportional constant. Different values of the exponent (n) give information about the types of interactions, such that the values of exponent n = 6, 8, and 10 represent dipole to dipole, dipole to quadrupole, and quadrupole to quadrupole interactions, respectively [154,155]. The graph of $log(I/x)$ versus $log(x)$ is depicted in Fig. 4.10 which is fitted by a linear equation ($y = mx + c$). The slope (m) of this fitted line gives a value of n/3, which is 1.89. Thus the value of n is ~5.7 which is near 6, so the dipole-to-dipole interaction of Tb^{3+} ions is responsible for the quenching phenomena.

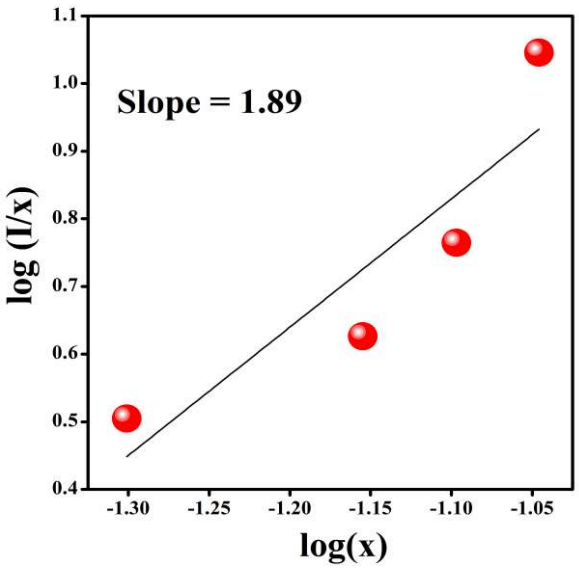

Fig. 4.9 log (I/x) versus log (x) plot for multi-polar interaction.

4.2.6.3 Energy transfer mechanism and PL decay analysis

The energy transfer process between Bi^{3+} to Tb^{3+} ions is explained in Fig. 4.11. Fig. 4.11(a) depicts the PLE spectra of T5 and B4 samples by monitoring the transition $^5D_4 \rightarrow {}^7F_5$ (544 nm) of Tb^{3+} emission. The obtained excitation band centered at 290 nm for the T5 sample is due to the overlapping of the LMCT band and the CTB band of Tb^{3+} ions. The excitation band of the B4 sample splits into two symmetric bands, one of which is an additional symmetric band at 323 nm because of the excitation transition $^1S_0 \rightarrow {}^3P_1$ of the Bi^{3+} ions. This suggests that the emission transition of Tb^{3+} is also achieved by the excitation of the Bi^{3+} ion (323 nm). Fig. 4.11(c) shows the emission spectra of T5 and B4 under Bi^{3+} excitation (323 nm). The emission intensity of Tb^{3+} transitions for the B4 phosphor is more intense than for the T5 phosphor which indicates that energy is transferring from the Bi^{3+} excited level to the equivalent Tb^{3+} excited levels. As a result, the population of excited electrons in the excited level of Tb^{3+} is increasing. Thereby, more photons are emitted due to the emission transition of Tb^{3+} ion and increase the intensity. The energy transfer mechanism between Bi^{3+} and Tb^{3+} is shown in Fig. 4.11(b) with the help of the Jablonski diagram of Bi^{3+} and Tb^{3+} ions.

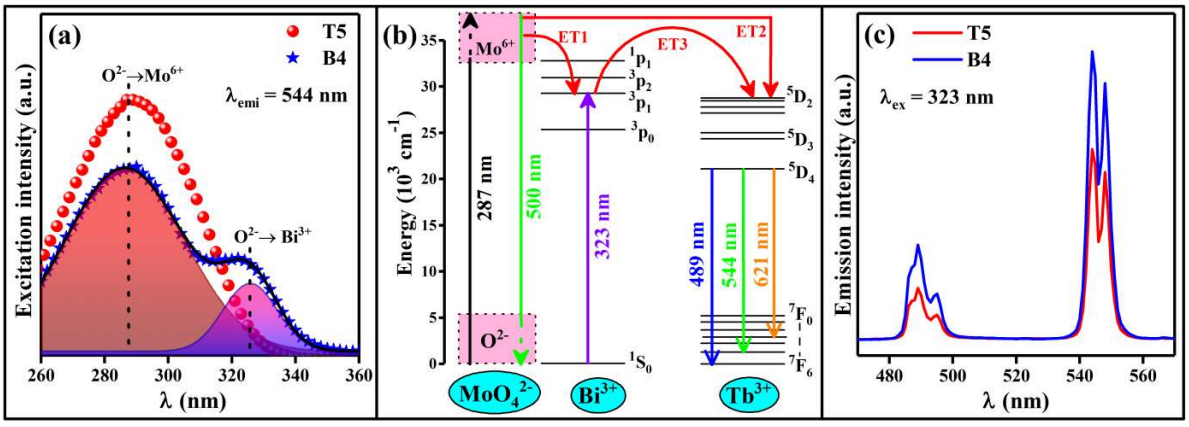

Fig. 4.10 (a) PL excitation, **(b)** Energy transfer mechanism, and **(c)** PL emission for T5 and B4 under Bi^{3+} excitations.

The normalized PL lifetime decay of the transition $^5D_4 \rightarrow {}^7F_5$ of Tb^{3+} ion for T5 and B4 samples under excitation of Bi^{3+} ion at 323 nm is depicted in Fig. 4.12(a). The lifetime decay is in good agreement with the following bi-exponential equation [156];

$$I(t) = I_0 + A_1 e^{\left(\frac{-t}{\tau_1}\right)} + A_2 e^{\left(\frac{-t}{\tau_2}\right)} \quad 4.7$$

where $I(t)$ and I_0 are the PL intensity at time t and long time, respectively. τ_1, τ_2 denote fast decay and slow decay times, and A_1, A_2 are their respective amplitudes. The average lifetime (τ_{av}) can be evaluated by following expression [156];

$$\tau_{av} = \frac{A_1\tau_1^2 + A_2\tau_2^2}{A_1\tau_1 + A_2\tau_2} \quad 4.8$$

The average decay lifetime of the T5 phosphor is 0.48 ms and for the B4 phosphor is 0.57 ms. The increase in the decay lifetime of the $^5D_4 \rightarrow {}^7F_5$ transition for the B4 sample is the result of an increase in electrons population in the $^5D_4$ excited level of the Tb^{3+} ion which may be mainly due to two reasons. The first reason may be transferring of charge from the excited Bi^{3+} ion to the $^5D_4$ level of the Tb^{3+} ion, and the second to the improvement of crystallinity with the doping of Bi^{3+} ion [135,157]. Improvement in crystallinity leads to a reduction in defect centers, thereby reducing the loss of absorption energy due to the reduction of these defects. As a result, the number of excited electrons increases[157,158]. The energy transfer process is evident from the PL emission obtained from Bi^{3+} excitation (323 nm), while the improvement in crystallinity on Bi^{3+} co-doping is evident from the XRD and SEM studies. Therefore, both of these factors may be possible for the increase in the population of excited electrons in the Tb^{3+} excited level ($^5D_4$). As a result, the emission intensity of Tb^{3+} has been increased.

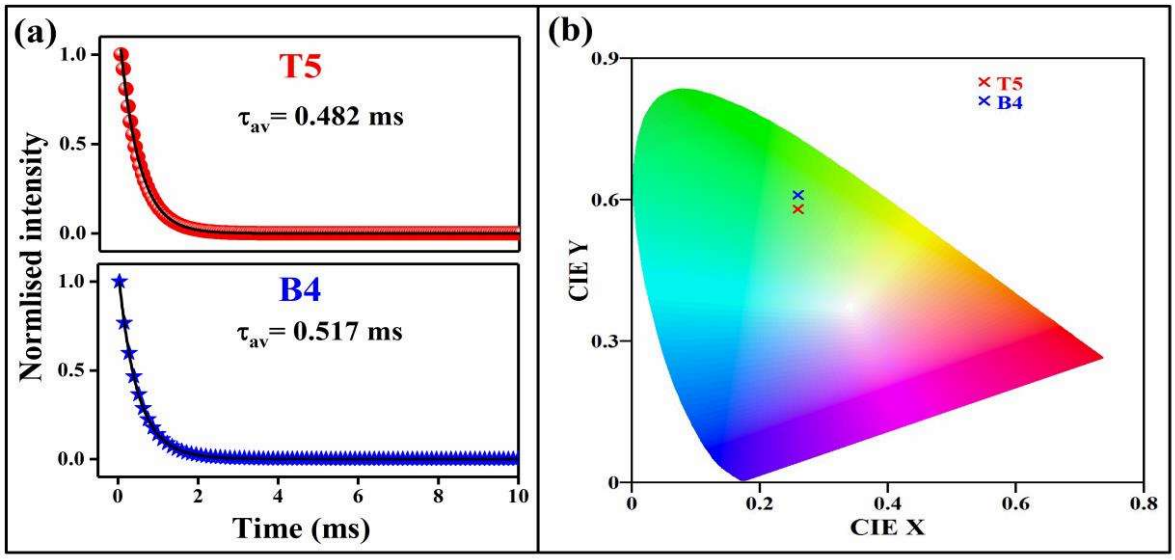

Fig. 4.11 (a) PL decays curves and **(b)** Chromaticity diagram for T5 and B4 phosphors.

4.2.7 Chromaticity parameters

The Commission Internationale l-Elcairage (CIE) coordinates of the T5 and B4 phosphors are marked in the chromaticity diagram (Fig. 4.12(b)) for the emission spectra from 380 nm to 750 nm. The obtained CIE coordinates for T5 are (0.267, 0.558). After Bi^{3+} co-doping, the CIE coordinates for B4 are 0.264, 0.604, shifted towards the green illuminated region. Thus, the chromaticity diagram depicts enhance in green color with Bi^{+3} co-doping.

Color purity (CP) refers to the mono chromaticity of the overall emitted light which is calculated by the following formula [37];

$$CP\ (in\ \%) = \sqrt{\frac{(x-x_o)^2+(y-y_o)^2}{(x_p-x_o)^2+(y_p-y_o)^2}} * 100 \qquad 4.9$$

where (x, y) is the CIE coordinates of the samples, (x_o, y_o) are the '1931 CIE standard' coordinates of the white illuminate point (0.3101, 0.3162), and (x_p, y_p) coordinates lie on the

perimeter which is found by extending a straight line drawn from (0.3101, 0.3162) to (x, y). The calculated value of CP for T5 and B4 phosphors are 51% and 64%, respectively. This enhancement suggests that the overall emission is shifted toward a greenish region.

Several phosphors have already been studied as green emitters, some of which are compared with the B4 sample in Table 4.3. The superior color purity and green CIE coordinates of the B4 phosphor indicate its excellent green-emitting phosphor.

Table 4.3 Comparison of CIE coordinates and color purity with Tb^{3+} doped other phosphors**.**

Tb^{3+} doped other phosphors	**CIE coordinates (x, y)**	**CP (%)**	**Ref.**
Tb^{3+} doped $Sr_2ZnSi_2O_7$	(0.266, 0.432)	21.8	[159]
Tb^{3+} doped Ba_2GeO_4	(0.270, 0.510)	38	[160]
Tb^{3+} doped $LaGaO_3$	(0.270, 0.526)	42.4	[161]
Na^+ /Tb^{3+} doped SrB_2O_4:Ce^{3+}	(0.301, 0.516)	46.5	[162]
Tb^{3+} doped $Ca_2YZr_2Al_3O_{12}$:Ce^{3+}	(0.261, 0.591)	59	[7]
B4 phosphor	(0.264, 0.604)	64	**This work**

4.2.8 Temperature-dependent PL (TDPL) analysis

The thermal stability for B4 phosphor has been studied by temperature-dependent PL (TDPL) in the limit of temperature 303 K to 503 K. Fig. 4.13(a) depicts the TDPL in which the intensity is continuously decreasing with temperature due to thermal quenching. However, no significant shift in the CIE coordinates is observed on temperature rises from 303 K to 503 K (Fig. 4.13(b)). Hence, there is no change in the emission color with temperature which suggests that B4 is thermally stable. Therefore, the B4 sample could become a potential phosphor in display lighting and anti-counterfeiting applications. The integrated emission intensity

obtained at 423 K becomes 76% of the integrated intensity at room temperature as depicted in Fig. 4.13(d). Hence, the intensity of emission at 423 K is decreased by 24% due to thermal quenching. The loss in intensity for B4 phosphor at 423 K is less than that of commercial YAG: Ce^{3+} phosphors and other previously reported phosphors [62,143,163,164].

The mechanism of thermal quenching is explained in Fig. 4.13(e) via the configurationally diagram, in which both the ground level and the exciting level are represented by the parabola and they intersect each other at point X. The interval between the bottom of the excited level the point X is the activation energy (E_a) required for thermal quenching. First of all, the ground-level electron reaches the excited state by absorbing the incident photon. The spin-lattice vibration at ambient temperature absorbs some of the electron energy which causes a non-radiative emission (1), after which the electron relaxes to an exciting equilibrium state. After this, the electrons revert to the ground level by the radiative transition (2). The strength of the lattice vibrations enhances with an increase in temperature, increasing thermally active phonons. Some of the electrons in the lower excited state come into contact with the active phonons and reach the intersection point X, due to which the electron returns to the ground state via the non-radiative transition (3). The result is thermal quenching in intensity[165,166]. This interaction between the electron and the phonon continues to increase with temperature, causing an enhancement in the number of electrons crossing the barrier height (E_a) and an increase in thermal quenching.

The activation energy (E_a) required for thermal quenching is evaluated by the following Arrhenius equation [165,166];

$$\frac{I_o}{I_T} = 1 + Ce^{\left(\frac{-E_a}{KT}\right)} \quad 4.10$$

Where I_o and I_T are the integrated emission intensity of the B4 phosphor at 303 K and T K, respectively. K is the Boltzmann constant. The activation energy is evaluated by linearly fitting the $ln\left(\frac{I_o}{I_T} - 1\right)$ versus $\frac{1}{KT}$ plot whose slope gives the information of activation energy, as depicted in Fig. 4.13(f). The obtained E_a value for the B4 phosphor is 0.25 eV which is higher than the other Tb^{3+} doped phosphors [162,167,168]. Higher activation energy means that more thermal energy will be required for quenching in intensity. Therefore B4 phosphor has good thermal stability making it a better candidate for wLED applications.

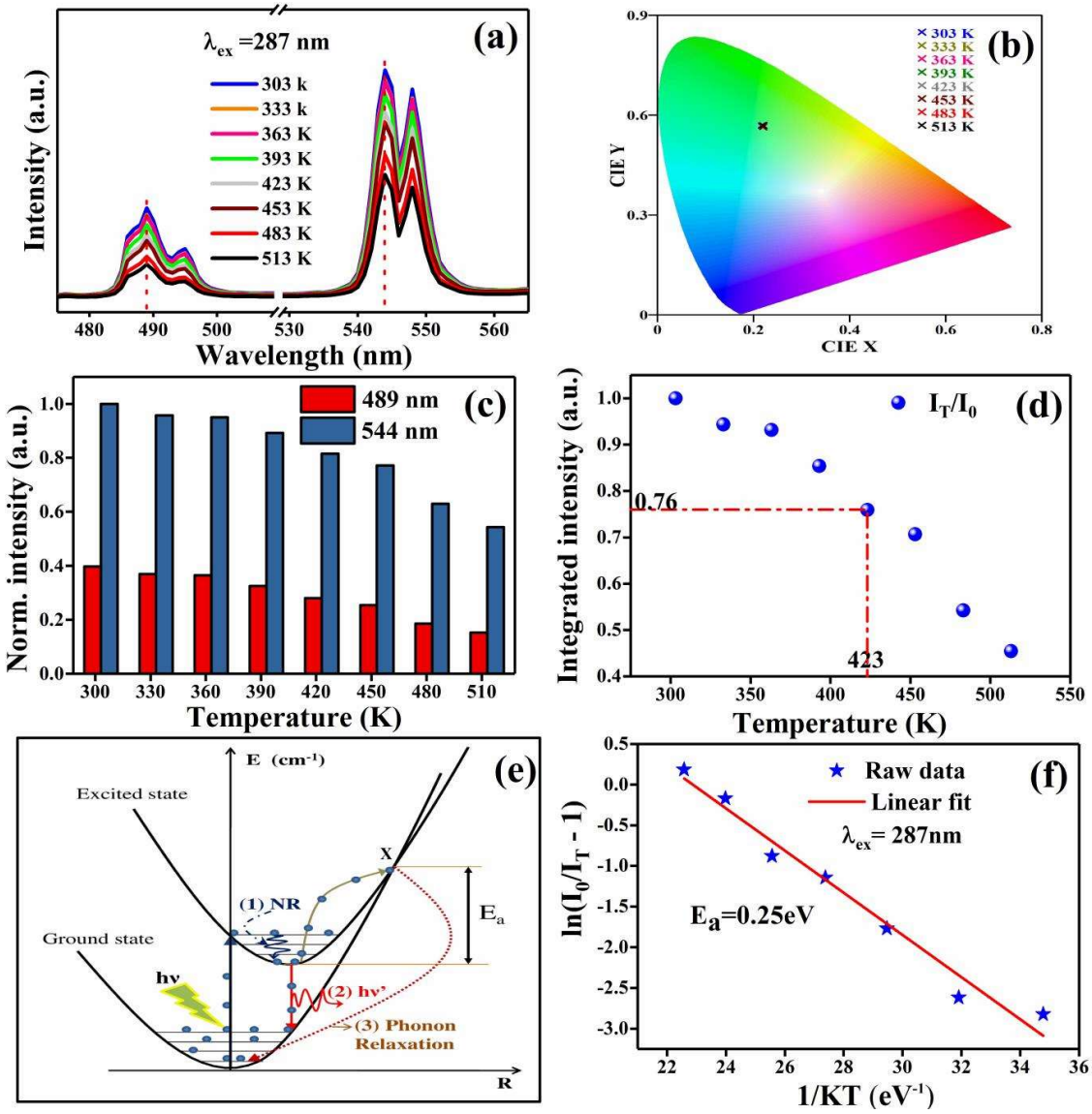

Fig. 4.12 (a) TDPL spectra for B4, **(b)** CIE coordinates variation with temperature, **(c)** Bar diagram depicting intensity variation, **(d)** Normalized integrated intensity versus temperature, **(e)** Configurationally diagram for explaining thermal quenching and **(f)** ln $[(I_o/I_T)-1]$ versus 1/KT graph for required activation energy calculation.

4.3 Conclusions

All phosphors have been successfully synthesized via the urea fueled-combustion method. The XRD patterns yield no impurity peak which confirms the successful substitution of doped elements at the calcium sites. The SEM images revealed the spherical shape of the particles

whose size increases with Bi^{3+} co-doping. Improvement in crystallinity establishes a correlation between structural studies and photoluminescence studies. Three prominent peaks in the Tb^{3+} doped $CaMoO_4$ phosphor under host excitation are observed in the PL emission spectra at 489 nm ($^5D_4 \rightarrow {}^7F_6$), 544 nm ($^5D_4 \rightarrow {}^7F_5$) and 621 nm ($^5D_4 \rightarrow {}^7F_3$), of which 544 nm (green emission) is the most intense. After Tb^{3+} doping, an enhancement in the emission spectra is observed up to the T5 phosphor which is further enhanced by Bi^{3+} co-doping. The co-doping of Bi^{3+} ion results in improved crystallinity in the phosphor as well as energy transferring from the Bi^{3+} exciting level to the Tb^{3+} excited level, which leads to an increase in luminescence. The maximum emission intensity of Tb^{3+} has been achieved at 4% Bi^{3+} co-doping (B4) giving excellent green emission. From the chromaticity diagram, it is articulated that the CIE coordinate of B4 is (0.264, 0.604) is shifted more to the green region than the T5 (0.267, 0.558). We have analyzed the temperature-dependent PL to the examination of thermal stability of the B4 phosphor and observed that it is a good thermally stable green phosphor with high activation energy (0.25 eV). The B4 phosphor exhibits only a 24% reduction in emission intensity at 423 K compared to room temperature, which is much less than the loss (~50%) at the same temperature as the well-known Ce^{3+} doped YAG yellow phosphor. No change was obtained in the CIE coordinates of the emission with temperature, indicating the color stability of the overall emission of the B4 phosphor. Thus, B4 phosphor is a capable candidate as a green phosphor for display devices and LEDs applications